Evaluation of eddy current damper for vibration control of a frame structure

Journal of Physics Communications

OPEN ACCESS

RECEIVED
7 February 2019

ACCEPTED FOR PUBLICATION
30 April 2019

PUBLISHED
15 May 2019

PAPER

Evaluation of eddy current damper for vibration control of a frame structure

Wai Kei Ao and Paul Reynolds

University of Exeter, Vibration Engineering section, College of Engineering, Mathematics and Physical Sciences, North Park Road, Exeter EX4 4QF, United Kingdom

E-mail: wka203@exeter.ac.uk **and** p.reynolds@exeter.ac.uk

Keywords: eddy current damper (ECD), permanent magnet, conductive material, unidirectional and alternative pole projection, electromagnetic forces, method of images current

Abstract

In this study, an eddy current damper (ECD) prototype model is presented. The ECD consists of three principal components: Neodymium Iron Boron (NdFeB) permanent magnets, a copper plate (conductive material) and an aluminium frame. The magnets have a rectangular design, and can be assembled with magnetic pole projection in either alternative or unidirectional orientations and in two orthogonal directions. The key merit of this type of ECD is its non-contact characteristic; thus there is a complete absence of mechanical friction. This study examines the use of this prototype damper when applied to suppress structural vibration in multi-storey frame structure. To effectively estimate the damping performance of the ECD, simple analytical calculations involving both infinite and finite boundaries are proposed and illustrated in this paper. These can be compared against the results of more sophisticated finite element analysis (FEA). The conductive material can be defined to move in two orthogonal directions. Therefore, based on the four magnet configurations and two directions of motion of conductive material, a total of eight models were created for analysis and validated by the proposed designed formule. It was found that analysis based on the method of images provides a satisfactory estimation of the damping force, similar to that estimated using the FE model. This study also includes experimental testing of a prototype ECD applied to suppress vibration within a six-storey aluminium frame structure. This testing shows that the prototype ECD is able to provide a significant level of damping with performance comparable to that of an ideal conventional linear viscous damper.

1. Introduction of eddy current damper (ECD)

Vibration problems occur in a range of engineering structures and affect the stability of many systems as well as creating serviceability issues. In civil engineering potential solutions were proposed, which commonly involved the addition of damping devices, for example viscous dampers (VDs), tuned mass dampers (TMDs), viscoelastic dampers (VEs) and friction dampers, to the primary system, in an attempt to change the system damping. From a civil engineering perspective, vibration suppression technologies pose a particular challenge due to the large-scale structures often involved to mitigate annoying vibrations, civil engineering structures are typically on a much larger scale and thus require the design of damping mechanisms to reflect the scale of such structures.

As an alternative to the use of traditional vibration suppression devices, a novel eddy current damper (ECD) is proposed to suppress mechanical system vibration. The design utilises the relative motion between a permanent magnet and conductor to create a resistive force. A simple example of an ECD is shown in [1]. It uses a neodymium magnet dropping through a conductive tube. This kind of simple model illustrates a damping mechanism opposing motion based on fundamental electromagnetic induction theory. A braking system consisting of a cylindrical magnet and arbitrary shaped conductor plate was presented in [2–4] to provide eddy

current damping according to their relative motion, including a simple theoretical study with an infinite boundary condition and using a rectangular magnet.

Eddy current damping was also introduced to reduce rotational motion [5–7]. The induced electric field intensity relies on geometric boundary conditions. Coulomb's law and Lorentz force law were introduced to tackle the braking torque calculation. The method of images current was applied to the torque validation with regard to considering the finite boundary condition of the conductor. Alternative ECD prototypes have also been suggested, such as a high capacity torque ECD, by [8], and a magnetic shock absorber and eddy current damping transformer by [9–11]. Additional studies can be found in [12] regarding the suppression of turbine blade vibration in a gas and steam system

In addition, a theoretical study of the rectangular magnet ECD prototype was presented in [13, 14] which used different rectangular magnetic pole orientation, resulting in different damping capacities being produced, corresponding to the varying flow of the eddy currents. This paper examined the phenomenon of magnetic pole projection by selecting various magnet configurations with different orientations to investigate the associated eddy current damping produced.

Some examples have been used in civil engineering. In [15–17], a non-contact ECD was used to suppress vibration in a cantilever beam and thin-walled frame, without any change to the system mass and stiffness. It was subsequently discovered that this type of non-contact damping results in enhanced system dynamics. With regard to the use of traditional large-scale TMDs for suppression of vibration, while a TMD can often offer a simple yet suitable solution, this is typically achieved through viscous damping which has various inherent issues such as oil leakage and non-adjustable damping post installation. Therefore, an ECD, as proposed by [18], could be applied to large-scale vibration control by using eddy current damping in an optimally designed TMD. Alternatively, in [19], a basic theoretical and experimental study of a magnetic TMD was conducted, which incorporated the use of a large-scale ECD to control vibration in a modelled bridge structure.

In this study will base on the previous researcher's findings and presents a method for analysing the eddy current in a time-invariant scenario with a rectangular shape prototype such as damping force design formula with infinite and finite boundary condition. Firstly, the fundamentals of electromagnetic induction theory and calculation of eddy current in relation to rectangular magnet geometry, along with an overview of the different directions of motion of the conductive plate and different layouts of magnetic pole projection for single-magnet and four-magnet arrangements will be presented. Secondly, an introduction to the concept of the method of images current will be provided and an explanation of how this can be used to increase accuracy of the analytical calculation of electromagnetic force. Thirdly, the numerical construction of the eight ECD models, previously mentioned, and their respective quantified performance will be described. Finally, the rationale related to the selection of one of these models as the prototype is presented; the prototype is constructed and subjected to further experimental vibration control testing and analysis when installed in a six-storey aluminium frame structure.

2. ECD with rectangular magnet arrangement

The basic law of electromagnetism is Faraday's law, or electromagnetic induction, which explains how the relative motion between the magnetic field and conductor can change the magnetic flux linkage, thus inducing electromotive force (emf) along with accompanying induced current, or eddy current. In other words, Faraday's law describes the process of an electric generator converting mechanical energy into electrical energy. This paper examines the application of several rectangular ECD prototype configurations and the use of the corresponding induced energy as a damping mechanism for vibration suppression.

2.1. Modelling eddy currents and electromagnetic force of the ECD

figure 1 shows a rectangular conductive plate, which is assumed to have infinite dimensions [14, 15]. Adjacent to the conductive plate, there is a finite sized rectangular permanent magnet, the dimensions of which are: length $2a$ in length, width $2b$, and thickness t. Note that the magnet is rectangular in shape. The dimensions of length and width as a factor of 2 is beneficial to define the lower and upper bounds of finite integration as $-a$ to a and $-b$ to b. The gap between the magnet and conductive plate is assumed to be very small compared with the dimensions of the magnet.

The magnetic flux density, or magnetic field, is directed into the page as shown in figure 1. Therefore, the magnetic flux density is in the negative z direction. The vector of magnetic field $\boldsymbol{B}$ can thus be expressed as:

$$\boldsymbol{B} = B_x\boldsymbol{i} + B_y\boldsymbol{j} + (-B_z)\boldsymbol{k} \tag{1}$$

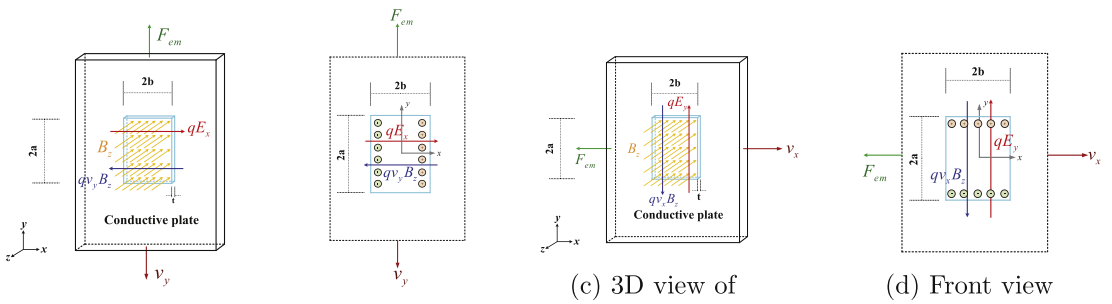

(a) 3D view of vertically moving conductive plate

(b) Front view with electrical charge moving in V_y

(c) 3D view of horizontally moving conductive plate

(d) Front view with electrical charge moving in V_x

Figure 1. Concept of generation of electromagnetic force via moving plate in a magnetic field.

where B_x, B_y and B_z are the individual components of magnetic flux density $\boldsymbol{B}$ in the x, y and z directions, respectively. Note that in this case, the magnetic flux density of the x and y components is zero, and hence only the z direction component contributes to the electromagnetic force.

In figure 1(c), the conductive plate is assumed to move in the positive x direction. Hence, the velocity vector $\boldsymbol{v}$ can be written as:

$$\boldsymbol{v} = v_x\boldsymbol{i} + v_y\boldsymbol{j} + v_z\boldsymbol{k} \tag{2}$$

In the case of the conductive plate moving in the x direction; v_y and v_z provide no contribution. Conversely, figure 1(a) shows the conductive plate moving in the negative y direction. The velocity vector can be written as:

$$\boldsymbol{v} = v_x\boldsymbol{i} + (-v_y)\boldsymbol{j} + v_z\boldsymbol{k} \tag{3}$$

It is noted that the other directional components v_x and v_z provide no contribution. In addition, all of these values are time-invariant.

The application of the fundamental electromagnetic theories is required. The magnetic flux density $\boldsymbol{B}$ is defined in terms of the force $\boldsymbol{F_B}$ acting on a charged particle q moving through the field with velocity $\boldsymbol{v}$; therefore, the magnetic force, or Lorentz force, on a charge q can be obtained as follows:

$$\mathbf{F_{em}} = q\mathbf{v} \times \mathbf{B} = \oint id\mathbf{l} \times \mathbf{B} = \int \mathbf{J} \times \mathbf{B}d\mathbf{V} \tag{4}$$

where i is current, $\boldsymbol{A}$ is the outward normal unit area vector, and $\boldsymbol{V}$ is the volume of magnetic pole projection. The term $\boldsymbol{J}$ can be defined as the current density (i.e. current per area). However, the current density can also be defined as the product of the conductivity of the material and the electric field.

The total electric field intensity induced in the conductive plate can be calculated as:

$$\boldsymbol{E} = \boldsymbol{E_{ind}} + \boldsymbol{E_v} = \boldsymbol{E_{ind}} + \boldsymbol{v} \times \boldsymbol{B} \tag{5}$$

where $\boldsymbol{E}$ is total electric field intensity. $\boldsymbol{E_{ind}}$ is the induced electric field intensity of the electric charge particle, and $\boldsymbol{E_v}$ is the electric field intensity caused by the magnetic flux density in addition to that of the charged particle, which is also the cross product of velocity and magnetic flux density. Current density can now be rewritten as follows:

$$\boldsymbol{J} = \sigma(\boldsymbol{E_{ind}} + \boldsymbol{E_v}) \tag{6}$$

It is noted that equation (6) describes the internal conductive plate condition, while the external conducting plate current density will provide no contribution to the magnetic field density, as given by:

$$\boldsymbol{J} = \begin{cases} \sigma(\boldsymbol{E_{ind}} + \boldsymbol{E_v}) & inside \\ \sigma\boldsymbol{E_{ind}} & outside \end{cases} \tag{7}$$

2.2. ECD using four potential magnetic pole projections

The magnetic pole projections can have different arrangements: unidirectional and alternative. Unidirectional pole projection refers to each magnet being oriented in the same direction, as opposed to alternative pole projection in which each magnet is oriented in a manner so that each N pole is aligned with an adjacent S pole. This concept was initially proposed by [14]; however, the study was limited to modelling the movement of a conductive plate in the horizontal plane within a framework of vertically configured magnets.

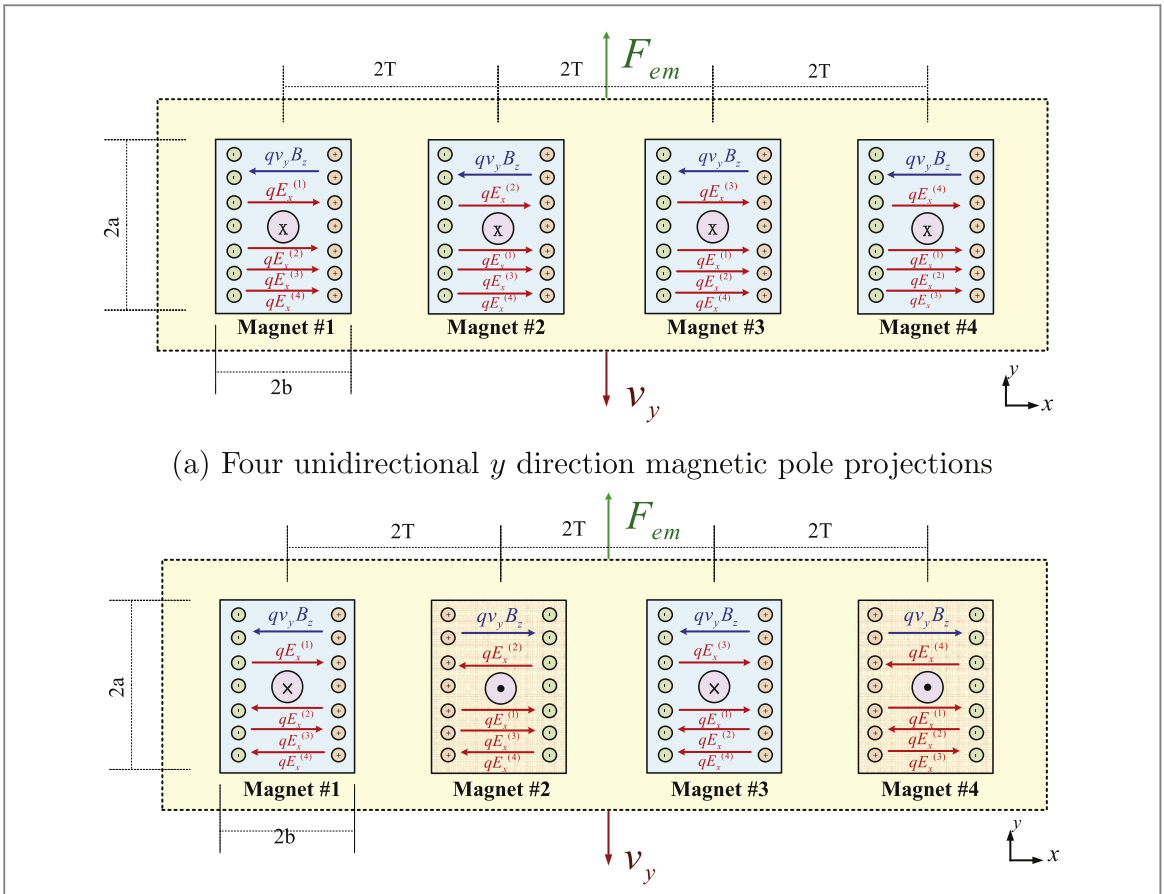

Figure 2. Electric field distribution of conductive plate moving in the *y* direction.

Apart from the unidirectional and alternative pole projection configurations, the magnet can also be aligned parallel to the *x* or *y* axis. The movement of the conductive plate in two directions (*x* or *y*) will be examined in this section. Hence, eight models of ECD will be examined in this study.

2.2.1. Conductive plate moving in the y *direction with magnets oriented in the* y *direction*

Figure 2(a) shows magnets aligned in the *y* direction. Note that the cross (×) sign convention refers to the magnetic flux density pointing inward in relation to the plane of the page. Figure 2(b) shows the alternative magnetic pole projection, in which the pole orientation of adjacent magnets are reversed. The dot (•) sign convention represents the magnetic flux density pointing outward from the page.

The dimensions of one magnetic pole projection can be defined by width 2*b* and height 2*a*. The distance between two pole projections centre-to-centre is 2*T*. The conductive plate can move in the *x* and *y* directions.

Figure 2(a) shows the conductive plate moving in the *y* direction and four unidirectional magnets aligned in the *y* orientation. With regard to the first magnet, it can be seen that the corresponding magnetic force qv_yB_z points to the left-hand side of the pole projection. The direction is based on the cross product right-hand rule of moving velocity and magnetic flux density. However, the first magnet also experiences another four different electric forces: $qE_y^{(1)}$, $qE_y^{(2)}$, $qE_y^{(3)}$, $qE_y^{(4)}$, where each numerical identifier corresponds to the relative magnet. As can be seen, all forces point to the right-hand side. In line with the concept of surface and linear charge density [5], it is possible to express the relevant electric intensities as:

$$\boldsymbol{E}_{\boldsymbol{x}}^{(n+1)} = E_x^{(n+1)}\boldsymbol{i} = -\frac{v_y B_z}{2\pi}\left[\begin{array}{l}\tan^{-1}\left(\frac{y-a}{x-b-2nT}\right) - \tan^{-1}\left(\frac{y+a}{x-b-2nT}\right) \\ +\tan^{-1}\left(\frac{y+a}{x+b-2nT}\right) - \tan^{-1}\left(\frac{y-a}{x+b-2nT}\right)\end{array}\right]_{n=0,1,2,3} \boldsymbol{i} \quad (8)$$

The electromagnetic force is the cross product of total current density and magnetic flux density. The force of the four unidirectional magnetic pole projections can be obtained as follows:

$$\boldsymbol{F_{em,y}} = F_{em,y}\boldsymbol{j} = -\sum_{n=1}^{4}\int \sigma(E_{ind,x} + v_y B_z)B_Z\, d\boldsymbol{V}\boldsymbol{j}$$
$$= -\sum_{n=1}^{4}\int \sigma(E_x{}^{(1)} + E_x{}^{(2)} + E_x{}^{(3)} + E_x{}^{(4)} + v_y B_z)B_z\, d\boldsymbol{V}\boldsymbol{j} \quad (9)$$

When the thickness of the conductive plate is known, the triple integral becomes a double integral. The relative integral boundary can be defined within the x and y dimensions of the pole projection; thus, the above damping force integration can be rewritten as

$$\boldsymbol{F_{em,y}} = F_{em,y}\boldsymbol{j} = -\sum_{n=1}^{4} t\int_{-a}^{a}\int_{-b}^{b} \sigma(E_x{}^{(1)} + E_x{}^{(2)} + E_x{}^{(3)} + E_x{}^{(4)} + v_y B_z)B_z\, dxdy\boldsymbol{j} \quad (10)$$

Figure 2(b) shows the alternative pole projection configuration, with the conductive plate moving in the y direction. Similarly, using the same method, the total electromagnetic force of the alternative pole projection configuration with the conductive plate moving in the y direction can be expressed as:

$$\boldsymbol{F_{em,y}} = F_{em,y}\boldsymbol{j} = -\sum_{n=1}^{4} t\int_{-a}^{a}\int_{-b}^{b} \sigma(E_x{}^{(1)} - E_x{}^{(2)} + E_x{}^{(3)} - E_x{}^{(4)} + v_y B_z)B_z\, dxdy\boldsymbol{j} \quad (11)$$

Note that the electric forces of the second and fourth magnetic pole projections point in the opposite direction to that of the first and third magnet pole projections; hence, the negative sign convention is applied to the second and fourth terms in equation (11).

2.2.2. Conductive plate moving in the x *direction with magnets oriented in the* y *direction*

The electromagnetic force and all the electric forces illustrated can be represented as follows:

$$\boldsymbol{F_{em,x}} = F_{em,x}\boldsymbol{i} = -\sum_{n=1}^{4} t\int_{-a}^{a}\int_{-b}^{b} \sigma(E_y{}^{(1)} - E_y{}^{(2)} + E_y{}^{(3)} - E_y{}^{(4)} + v_x B_z)B_z\, dxdy\boldsymbol{i} \quad (12)$$

where

$$\mathbf{E_y^{(n+1)}} = E_y{}^{(n+1)}\mathbf{j} = -\frac{v_x B_z}{2\pi}\left[\begin{array}{l}\tan^{-1}\left(\frac{x-b}{y-a-2nT}\right) - \tan^{-1}\left(\frac{x+b}{y-a-2nT}\right)\\ -\tan^{-1}\left(\frac{x-b}{y+a-2nT}\right) + \tan^{-1}\left(\frac{x+b}{y+a-2nT}\right)\end{array}\right]_{n=0,1,2,3}\mathbf{j} \quad (13)$$

It can be observed that this case is similar to that of the previous alternative pole projection. With regard to the first magnetic pole projection, the second and fourth electric forces point in the downside direction, opposite to that of the first and third electric forces. Therefore, this downside direction is reflected by the negative sign convention for the relative electric intensity. However, in the case of the unidirectional pole projection, the $F_{em,x}$ can be derived by changing the negative sign of $-E_y^2$ and $-E_y^4$ of the equation (12) to positive sign (E_y^2 and E_y^4).

Similarly, the aforementioned process can also derive correlated genral induced electric intensity when conductive plate moving in the y and x directions with magnets oriented in the x direction. The derivation detail can be referenced by [20].

3. Eddy current method of images

3.1. Eddy current method of images for single magnet

The previous section dealt with the case of a conductive plate with infinite x and y dimensions. In this section, the eddy current image method [15, 21] is discussed as a means to calculate the ECD electromagnetic force using finite x and y dimensions, thus resulting in eddy currents with a value of zero at the edges of the conductive plate.

The solid line in figure 3 shows the infinite boundary condition of eddy current density $J^{(p)}$. The two tails of the curve extend infinitely in the positive and negative directions. Due to the finite dimensions of the plate, the actual current flowing is not precisely as represented by the curve; thus resulting in potentially erroneous results if used for calculation purposes.

To solve this problem, the tails of the profile of $\boldsymbol{J^{(P)}}$ are reflected about axes of symmetry corresponding with the edges of the conductive plate. In this case, the image current density on the left-hand edge ($\boldsymbol{J^{i_{left}}}$) is reflected to the right and the right-hand edge $\boldsymbol{J^{i_{right}}}$ is reflected to the left. Note that in the case of image current density, only the contribution of the external conductive plate is considered (as shown in equation (7)) and, therefore, the edge effect can be eliminated.

Therefore, when the conductive plate moves in the y direction, the relationship between the primary and image current density can be expressed as:

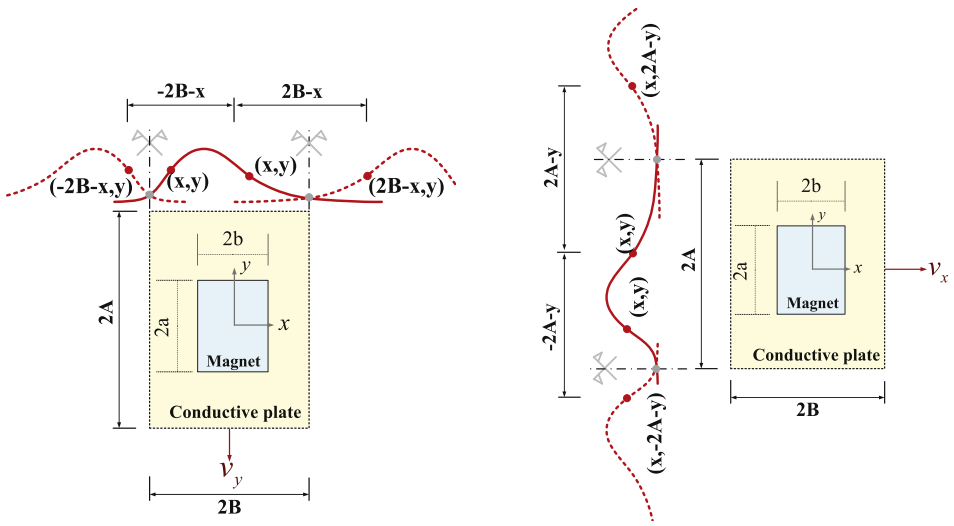

(a) Single magnetic pole projections with conductive plate moving in the y direction

(b) Single magnetic pole projections with conductive plate moving in the x direction

Figure 3. Eddy current density using method of images current for conductive plate moving in the y and x direction.

$$\boldsymbol{J_x'} = J_x'\boldsymbol{i} = J_x^{(P)}\boldsymbol{i} - J_x^{(i_{right})}\boldsymbol{i} - J_x^{(i_{left})}\boldsymbol{i} \tag{14}$$

The eddy image current density and primary eddy current density are symmetrical. In terms of the y movement of the conductive plate, $\boldsymbol{J_{left}^{i}}$ can be expressed in terms of $\boldsymbol{J^{(P)}}$ by using coordinate transformation, as given by:

$$J_x^{(i_{left})}\boldsymbol{i} = J_x^{(P)}(-2B - x, y)\boldsymbol{i}$$
$$= \sigma\left\{-\frac{v_y B_z}{2\pi}\left[\tan^{-1}\left(\frac{y-a}{-2B-x-b}\right) - \tan^{-1}\left(\frac{y+a}{-2B-x-b}\right) + \tan^{-1}\left(\frac{y+a}{-2B-x+b}\right) - \tan^{-1}\left(\frac{y-a}{-2B-x+b}\right)\right]\right\}\boldsymbol{i} \tag{15}$$

The same method can be used to express $\boldsymbol{J_{right}^{i}}$ in terms of $\boldsymbol{J^{(P)}}$, as given by:

$$J_x^{(i_{right})}\boldsymbol{i} = J_x^{(P)}(2B - x, y)\boldsymbol{i}$$
$$= \sigma\left\{-\frac{v_y B_z}{2\pi}\left[\tan^{-1}\left(\frac{y-a}{2B-x-b}\right) - \tan^{-1}\left(\frac{y+a}{2B-x-b}\right) + \tan^{-1}\left(\frac{y+a}{2B-x+b}\right) - \tan^{-1}\left(\frac{y-a}{2B-x+b}\right)\right]\right\}\boldsymbol{i} \tag{16}$$

Following determination of the resulting new eddy current density, it can be substituted into equation (4) in order to calculate the electromagnetic force produced by $\boldsymbol{J_{x'}}$, which can be expressed as:

$$\boldsymbol{F_{em,y}} = F_{em,y}\boldsymbol{j} = \int J_{x'} \times B_z dVj = t\int_{-a}^{a}\int_{-b}^{b}(J_x^{(P)} - J_x^{(i_{right})} - J_x^{(i_{left})})B_z dxdy\boldsymbol{j} \tag{17}$$

The eddy current method of images can be applied in a similar manner for the case of moving the conductive plate in the x direction, as shown in figure 3(b), which results in the total updated eddy current density in the y component being expressed as follows:

$$\boldsymbol{J_{y'}} = J_y'\boldsymbol{j} = J_y^{(P)}\boldsymbol{j} - J_y^{(i_{right})}\boldsymbol{j} - J_y^{(i_{left})}\boldsymbol{j} \tag{18}$$

where the application of coordinate transformation shifts the primary eddy current density $\boldsymbol{J_y^{(P)}}$ to locations $(x,\ 2A - y)$ and $(x,\ -2A - y)$, as given by equations (19) and (20), respectively:

$$J_y^{(i_{right})}\boldsymbol{j} = J_y^{(P)}(x,\ 2A - y)\boldsymbol{j}$$
$$= \sigma\left\{-\frac{v_x B_z}{2\pi}\left[\tan^{-1}\left(\frac{x-b}{2A-y-a}\right) - \tan^{-1}\left(\frac{x+b}{2A-y-a}\right) + \tan^{-1}\left(\frac{x-b}{2A-y+a}\right) - \tan^{-1}\left(\frac{x+b}{2A-y+a}\right)\right]\right\}\boldsymbol{j} \tag{19}$$

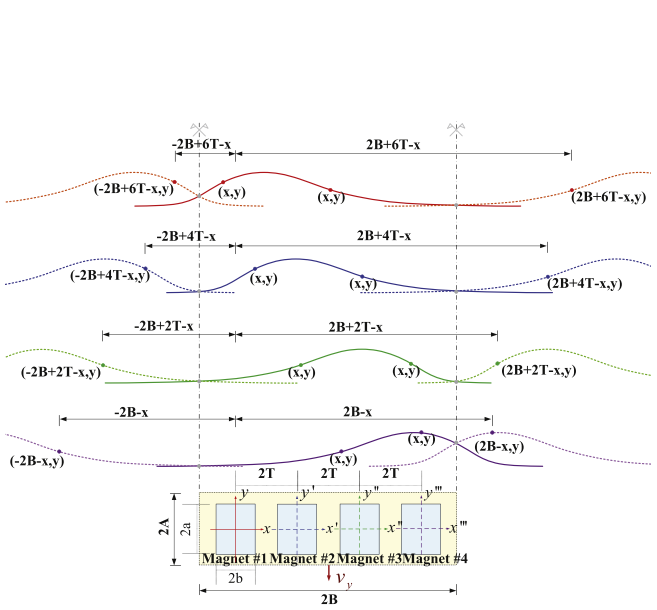

(a) Four y direction magnetic pole projections for conductive plate moving in the y direction

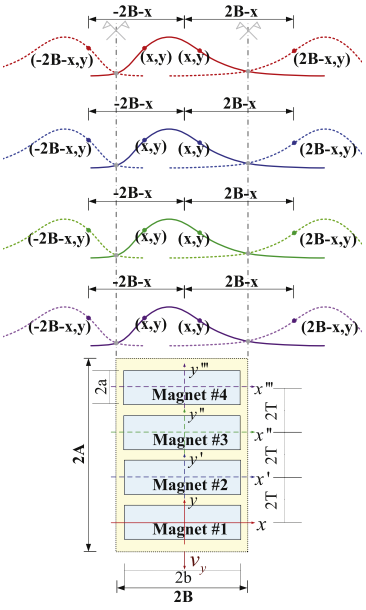

(b) Four x direction magnetic pole projections conductive plate moving in the y direction

Figure 4. Eddy current density of four magnetic pole projections using the eddy current image method for conductive plate moving in the y direction.

$$J_y^{(i_{left})}\boldsymbol{j} = J_y^{(P)}(x, -2A - y)\boldsymbol{j}$$
$$= \sigma\left\{-\frac{v_x B_z}{2\pi}\left[\tan^{-1}\left(\frac{x-b}{-2A-y-a}\right) - \tan^{-1}\left(\frac{x+b}{-2A-y-a}\right) + \tan^{-1}\left(\frac{x-b}{-2A-y+a}\right) - \tan^{-1}\left(\frac{x+b}{-2A-y+a}\right)\right]\right\}\boldsymbol{j} \tag{20}$$

Hence, the total eddy current density in the x direction is the combination of $J_y^{(P)}\boldsymbol{j}$, $J_y^{(i_{right})}\boldsymbol{j}$ and $J_y^{(i_{left})}\boldsymbol{j}$; the result of which allows the electromagnetic force to be determined as:

$$\boldsymbol{F_{em,x}} = F_{em,x}\boldsymbol{i} = -\int J_y' \times B_z dVi = -t\int_{-a}^{a}\int_{-b}^{b}(J_y^{(P)} - J_y^{(i_{right})} - J_y^{(i_{left})})B_z dxdy\boldsymbol{i} \tag{21}$$

3.2. Eddy current method of images for four magnet configuration

This section describes how an eddy current method of images [15, 21] is applied in the case of the four magnetic pole projections to determine a more precise total eddy current density, which facilitates calculation of the resultant electromagnetic (damping) force.

3.2.1. Conductive plate moving in the y *direction with four magnets oriented in the* y *direction*

In this case, the movement of the conductive plate in the y direction for the four magnetic pole projections in the y direction produces electromagnetic coupling between each magnet and the conductive plate, resulting in the generation of eddy currents. The solid line shown in figure 4(a) indicates the infinite boundary condition of the eddy current density. The coordinate system defines the middle of the first magnet. As discussed previously, the infinite boundary can potentially give rise to erroneous calculations with regard to the electromagnetic force. Therefore, the eddy current method of images is applied to refine the primary current density.

The tails of the profile of $\boldsymbol{J}^{(P)}$ are reflected about axes of symmetry corresponding to the edges of the conductive plate. In this four-magnet case, the image current densities are located as follows: magnet 1 at $(6T \pm 2B - x, y)$, shown in red; magnet 2 at $(4T \pm 2B - x, y)$, shown in blue; magnet 3 at $(2T - \pm 2B - x, y)$, shown in green; and magnet 4 at $(\pm 2B - x, y)$, shown in purple. The sum of the primary current density and all image current densities is used to determine the updated total eddy current density of the alternative magnetic pole projection configuration, given by:

$$\begin{aligned}\boldsymbol{J}_x' &= J_x'\boldsymbol{i} = J_x^{(P)}\boldsymbol{i} - J_x^{(i_{right})}\boldsymbol{i} - J_x^{(i_{left})}\boldsymbol{i}\\ &=[J_v + (-J_x^{(1)} + J_x^{(2)} - J_x^{(3)} + J_x^{(4)})]\boldsymbol{i}\ldots\\ &-[-J_x^{(1)}(6T - 2B - x, y) + J_x^{(2)}(4T - 2B - x, y) - J_x^{(3)}(2T - 2B - x, y) + J_x^{(4)}(-2B - x, y)]\boldsymbol{i}\ldots\\ &-[-J_x^{(1)}(6T + 2B - x, y) + J_x^{(2)}(4T + 2B - x, y) - J_x^{(3)}(2T + 2B - x, y) + J_x^{(4)}(2B - x, y)]\boldsymbol{i}\end{aligned} \tag{22}$$

where the J_v represents $v_y \times B_z$, and $J_x^{(1)}$, $J_x^{(2)}$, $J_x^{(3)}$ and $J_x^{(4)}$ are used to multiply σ in equation (8), corresponding to the magnet number.

However, the updated unidirectional total eddy current density changes the sign convention of the current density of the second and fourth magnet to negative, which can then be rewritten as follows:

$$\begin{aligned}\boldsymbol{J}_x' &= J_x'\boldsymbol{i} = J_x^{(P)}\boldsymbol{i} - J_x^{(i_{right})}\boldsymbol{i} - J_x^{(i_{left})}\boldsymbol{i}\\ &=[J_{ind} + (-J_x^{(1)} - J_x^{(2)} - J_x^{(3)} - J_x^{(4)})]\boldsymbol{i}\ldots\\ &-[-J_x^{(1)}(6T - 2B - x, y) - J_x^{(2)}(4T - 2B - x, y) - J_x^{(3)}(2T - 2B - x, y) - J_x^{(4)}(-2B - x, y)]\boldsymbol{i}\ldots\\ &-[-J_x^{(1)}(6T + 2B - x, y) - J_x^{(2)}(4T + 2B - x, y) - J_x^{(3)}(2T + 2B - x, y) - J_x^{(4)}(2B - x, y)]\boldsymbol{i}\end{aligned} \tag{23}$$

3.2.2. Conductive plate moving in the y *direction with four magnets oriented in the* x *direction*

figure 4(b) shows the configuration with four x direction magnetic pole projections, in which the conductive plate moves in the y direction, and the coordinate system indicates the middle of the bottom magnet. Application of the eddy current method of images results in the two tails of the primary eddy current density profile being reflected on the axes of the two edges of the conductive plate. As all magnetic pole projections are aligned in parallel, a common symmetrical centre is shared by all magnets. Therefore, all image currents have the consistent new coordinate $(\pm 2B - x, y)$. The corresponding updated total eddy current density of the alternative magnetic pole projection can be determined as follows:

$$\begin{aligned}\boldsymbol{J}_x' &= J_x'\boldsymbol{i} = J_x^{(P)}\boldsymbol{i} - J_x^{(i_{right})}\boldsymbol{i} - J_x^{(i_{left})}\boldsymbol{i}\\ &= [J_{ind} + (-J_x^{(1)} + J_x^{(2)} - J_x^{(3)} + J_x^{(4)})]\boldsymbol{i}\ldots\\ &- [-J_x^{(1)}(2B - x, y) + J_x^{(2)}(2B - x, y) - J_x^{(3)}(2B - x, y) + J_x^{(4)}(2B - x, y)]\boldsymbol{i}\ldots\\ &- [-J_x^{(1)}(-2B - x, y) + J_x^{(2)}(-2B - x, y) - J_x^{(3)}(-2B - x, y) + J_x^{(4)}(-2B - x, y)]\boldsymbol{i}\end{aligned} \tag{24}$$

When the magnetic pole projections are arranged in a unidirectional orientation, the updated total eddy current density is rewritten as follows:

$$\begin{aligned}\boldsymbol{J}_x' &= J_x'\boldsymbol{i} = J_x^{(P)}\boldsymbol{i} - J_x^{(i_{right})}\boldsymbol{i} - J_x^{(i_{left})}\boldsymbol{i}\\ &= [J_{ind} + (-J_x^{(1)} - J_x^{(2)} - J_x^{(3)} - J_x^{(4)})]\boldsymbol{i}\ldots\\ &- [-J_x^{(1)}(2B - x, y) - J_x^{(2)}(2B - x, y) - J_x^{(3)}(2B - x, y) - J_x^{(4)}(2B - x, y)]\boldsymbol{i}\ldots\\ &- [-J_x^{(1)}(-2B - x, y) - J_x^{(2)}(-2B - x, y) - J_x^{(3)}(-2B - x, y) - J_x^{(4)}(-2B - x, y)]\boldsymbol{i}\end{aligned} \tag{25}$$

Clearly, the eddy current density of the unidirectional magnetic pole projections requires changing all sign conventions to negative, and the results can be substituted into equation (17) to calculate the resultant electromagnetic (damping) force.

The Eddy current density of conductive plate moving in the x direction with four magnets oriented in the x and y directions can also be derived as the aforementioned process. The detail can be referenced by [20].

4. ECD prototype

4.1. Comparison between theoretical and finite element model results

To understand further the fundamental prediction of the generating force, finite element analysis (FEA) is conducted to verify the analytical results, through the use of ANSYS Maxwell electromagnetic field simulation software.

Figure 5 shows the magnets oriented in the y direction. The y direction configuration also defines two types of pole projection. Figure 5(a) shows the alternative magnetic pole projection configures so that the N pole is placed adjacent to the S pole. However, figure 5(b) shows the unidirectional magnetic pole projection, in which all the poles are configured in the same direction. The distance between two magnet cores is defined as $2T$ and t_{gap} represents the distance between two magnet panels. Figure 5(c) shows the side view of the ECD, illustrating how the movement of the copper plate (conductive material) through this gap causes the disruption of the magnetic lines.

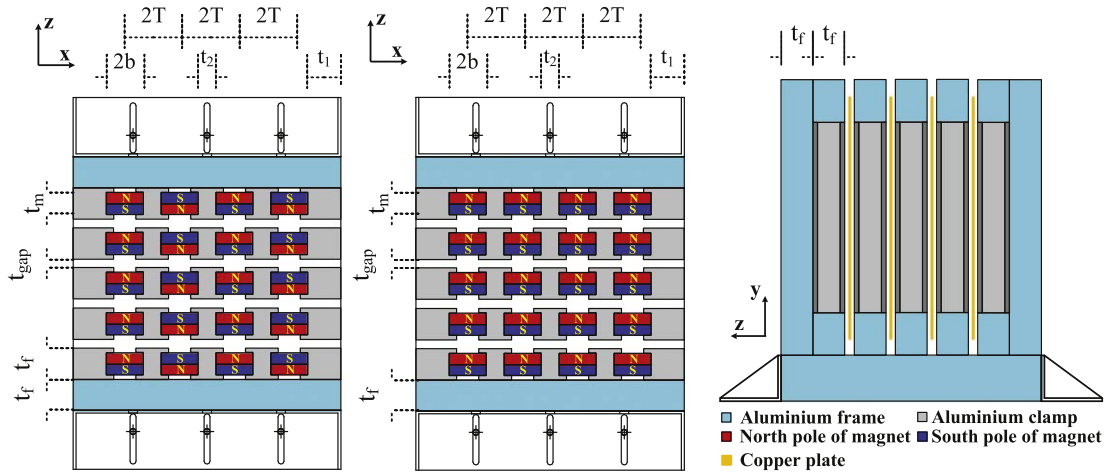

(a) Top view of ECD y direction alternative pole projection magnet layout

(b) Top view of ECD y direction unidirectional pole projection magnet layout

(c) Side view of ECD y direction pole projection magnet layout

Figure 5. ECD y direction alternative and unidirectional pole projection magnet layout.

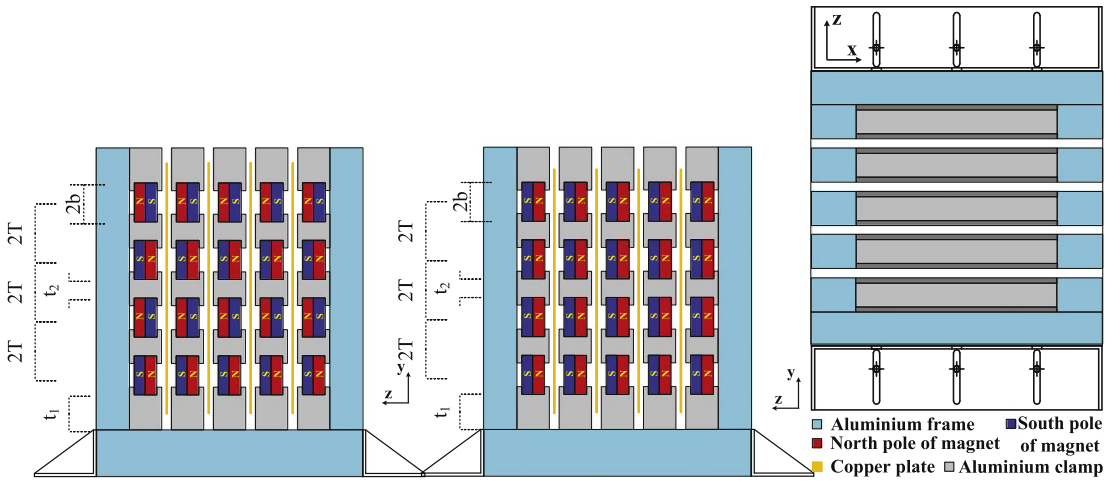

(a) Top view of ECD x direction alternative pole projection magnet layout

(b) Top view of ECD horizontal unidirectional pole projection magnet layout

(c) Side view of ECD x direction pole projection magnet layout

Figure 6. ECD x direction alternative and unidirectional pole projection magnet layouts.

An alternative magnet configuration, in which the magnets are configured in the x direction, is also considered as shown in figure 6. Figure 6(a) shows the alternative pole projection of the x direction magnet, while figure 6(b) shows the unidirectional magnetic pole projection. Figure 6(c) shows the top view of this configuration.

To employ the electromagnetic induction, a copper plate (conductive material) is moved into the gap between the two magnet panels, in the x and y direction. As mentioned previously, there are eight ECD models to be considered, and the following describes the FE analysis and analytical calculations associated with these eight models.

With regard to the construction of the ECD, the relevant dimensions are defined in table 1. The ECD has a total volume of 181 $\times$ 171 $\times$ 211 mm. The conductive material selected is copper in the form of a plate shape, with high electrical conductivity $\sigma = 5.8 \times 10^7\ 1/(\Omega \cdot \mathrm{m})$. The dimensions of the copper plate are 281 $\times$ 330 $\times$ 1 mm.

Table 1. Dimensions of constructed ECD.

	Description	(m)		Description	(m)
$2A$	length of copper plate	0.330	t	thickness of copper plate	0.001
$2B$	width of copper plate	0.281	t_m	thickness of magnet	0.015
$2T$	two core magnet distance	0.037	t_{gap}	two magnet panel distance	0.006
$2a$	length of magnet	0.125	t_1	Frame distance 1	0.022 5
$2b$	width of magnet	0.025	t_2	Frame distance 2	0.012

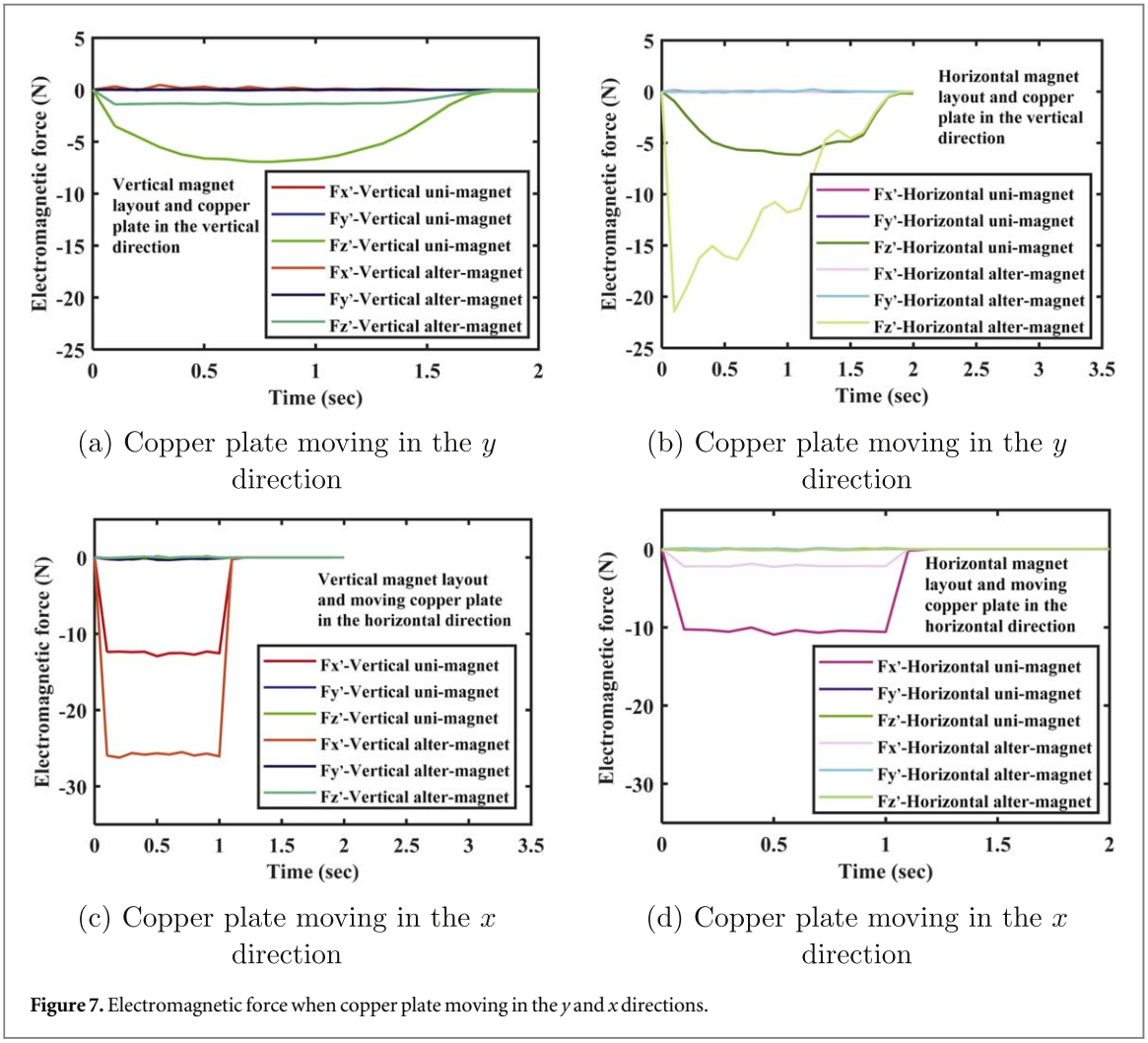

(a) Copper plate moving in the y direction

(b) Copper plate moving in the y direction

(c) Copper plate moving in the x direction

(d) Copper plate moving in the x direction

Figure 7. Electromagnetic force when copper plate moving in the y and x directions.

For the purpose of this study, a neodymium iron boron (NdFeB) Grade N42 magnet was selected. The nominal magnitude of magnetic flux density of N42 is 1.32 T. It is noted that a uniform distribution of magnetisation of the magnet (NdFeB) was assumed.

In the simulations, a constant magnitude velocity of 0.08 m s^{-1} was used; this reduces the time required for analysis, and the value is based on typical velocities from the AMRF study, which is presented in section 5. The analytical results obtained are compared later with the experimental results obtained. Figures 7(a) and (b) show the different magnitudes of the electromagnetic damping forces moving the copper plate in the y direction. As a result, the horizontal ($x = y'$) direction alternative magnetic pole projection configuration produces the largest electromagnetic force in the $y = z'$ direction. In contrast, the vertical ($y = z'$) direction alternative pole projection produces the smallest contribution to damping. Table 2 shows the theoretical and FE analysis results obtained for the relevant electromagnetic damping forces.

When the conductive plate is moved in the x direction, as shown in figures 7(c) and (d), the vertical ($y = z'$) direction alternative pole projection contributes the largest damping force in the horizontal ($x = y'$) direction, whereas the smallest damping force occurs in the $x = y'$ direction alternative pole projection configuration; the relevant results for these two cases can also be seen in table 2.

Table 2. Electromagnetic force calculation results.

		Electromagnetic force F_{em} (N)					
		Copper plate horizontal moving velocity Vx = 0.08 (m s^{-1})			Copper plate vertical moving velocity Vy = 0.08(m s^{-1})		
		Analytical calculation	ECIM	FEM results	Analytical calculation	ECIM	FEM results
Vertical Magnet	UPP	16.94	13.25	12.94	8.45	7.06	6.94
	APP	43.84	26.38	26.23	1.49	1.49	1.40
Horizontal Magnet	UPP	35.49	11.68	10.93	6.24	5.64	5.43
	APP	4.01	2.34	2.27	23.38	22.99	21.43

Note. ECIM = Eddy current image mthod; UPP = Unidirectional pole projection; APP = Alternative pole projection.

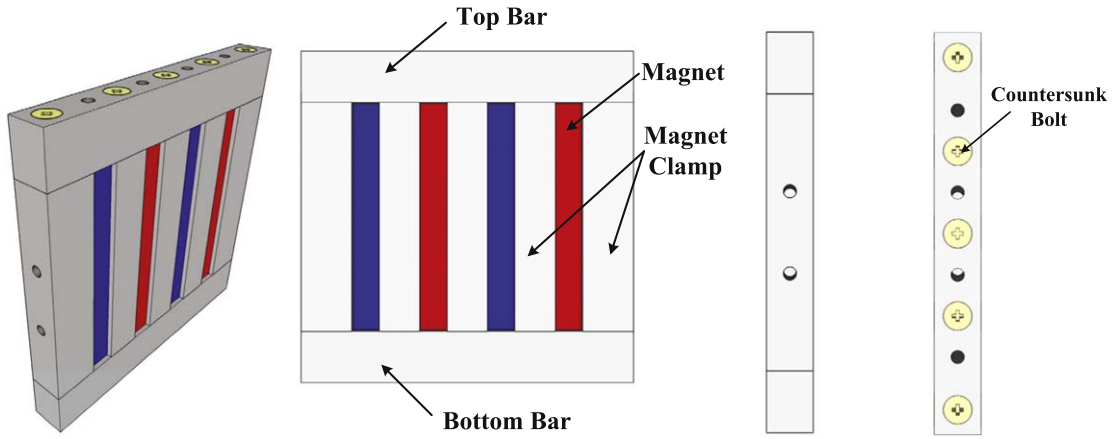

Figure 8. Magnet panel detail of ECD.

Notably, the contribution to damping force produced by the other two components is considered negligible for the purpose of this study.

To compare against the FEM results, the results obtained from analytical calculations, including the non-modified method and eddy current method of images, are also shown in table 2, where it can be seen that the initial analytical calculation results are normally higher than those obtained from the FEM. However, the results obtained by the eddy current method of images are close to those obtained from the FEM analysis. This indicates that the eddy current method of images is effective in eliminating the effect of the infinite boundary of the current density, but the magnetic field density is still assumed to have uniform distribution, which may still be a potential cause of slight error.

4.2. Construction of the ECD

Figure 8 shows the configuration of one of the magnet panels, the principal component of which is the permanent magnet (red = North Pole, blue = South Pole). To mount the magnet at its designed position, aluminium framing components were used and secured by countersunk bolts.

A similar construction was used to secure the other four magnet panels, along with the addition of top and bottom baseplates, as shown in figure 9, to maintain the vertical alignment of the magnet panels. A side plate was used to cover the outside of the magnet panels to provide protection and also reducing the possibility of magnetic fields influencing other devices. The angular plate mounted to the bottom baseplate provides for attachment to the structure on which the ECD is installed.

For this experimental work, copper plate was selected as the conductive material, used to induce the electromagnetic coupling. Four independent copper plates were mounted using clamp component, thus forming a single unit, as shown in figure 9. The copper plates and clamp are suspended from an L-shaped plate, which provides mounting place. Note that a load cell is connected between the copper clamp and the L-shape plate to directly measure the electromagnetic (damping) force.

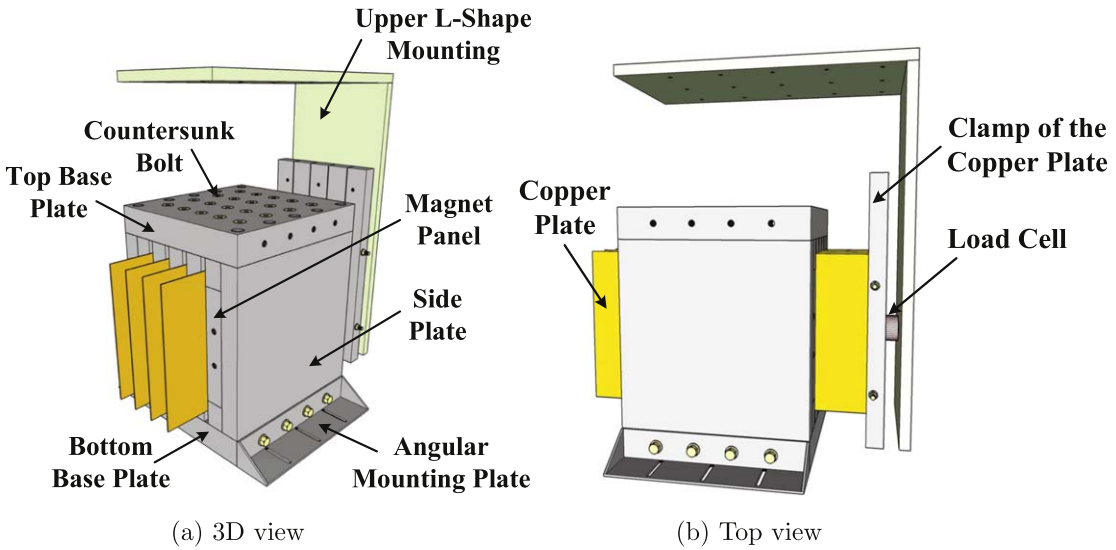

Figure 9. ECD schematic drawings.

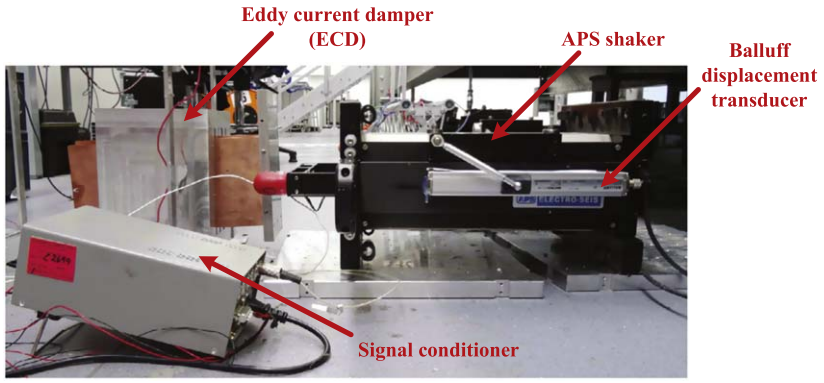

Figure 10. Photo of ECD performance test.

4.3. Experimental setup and practical study of the feedforward reference

Figure 10 shows a photo of the ECD performance test setup. The unloaded APS shaker lay on the ground in the horizontal direction to provide a force input. One side of the load cell and an accelerometer was connected to the armature of the APS shaker. The other side of the load cell was attached to the copper plate body unit. The four copper plates were located between the five magnet panels without any physical contact.

The displacement of the copper plate was measured using a Balluff position transducer. This also provided a feedforward reference tracking to track the ideal reference displacement input of the ECD, since the test was run using displacement control.

Figure 11 shows the practical control law of the feedforward reference [22]. The actuator was the control system (plant) in the control law. However, the dynamics of the actuator in this unloaded case was a constant 300 N/V, which is the relationship between the force and drive voltage. The high frequency noise effect was moderated by a second order Butterworth low-pass filter, which had a cut-off frequency at 50 Hz. A proportional derivative (PD) controller was used in the real-time feedback control to minimise the error value $E(s)$, the difference between desired input and measured output. Proportional and derivative gains of 0.000 1 and 0.01 were used, respectively, in the PD control.

4.4. Evaluation of ECD damping

After setting up the ECD performance test, a range of displacements of 7 mm, 8.75 mm, 10.5 mm, 12.25 mm and 14 mm were used for the displacement control. These displacements are the ideal reference input; the control loop tries to track this input displacement and minimise the error. For the different displacement amplitude reference inputs, sinusoidal signals with frequencies of 0.25 Hz, 0.5 Hz, 0.75 Hz, 1 Hz, 1.25 Hz, 1.5 Hz, 1.75 Hz and 2 Hz were used.

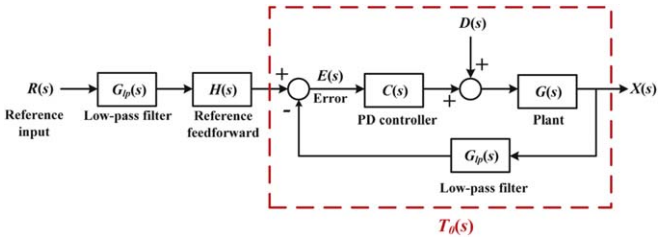

Figure 11. Feedforward reference control law of ECD performance test (after [22]).

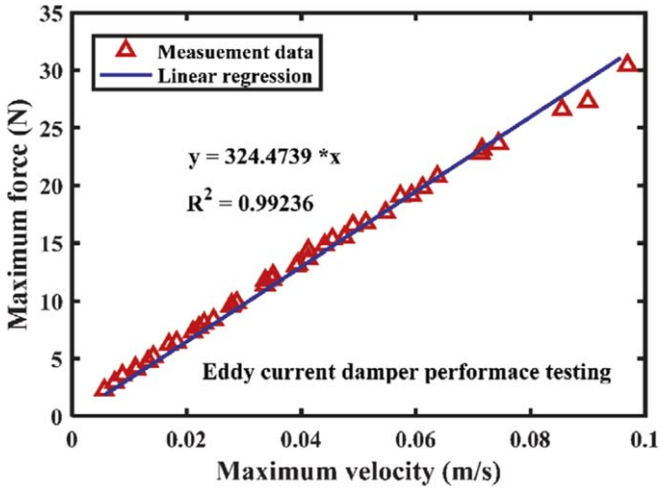

Figure 12. Linear regression of the ECD performance test.

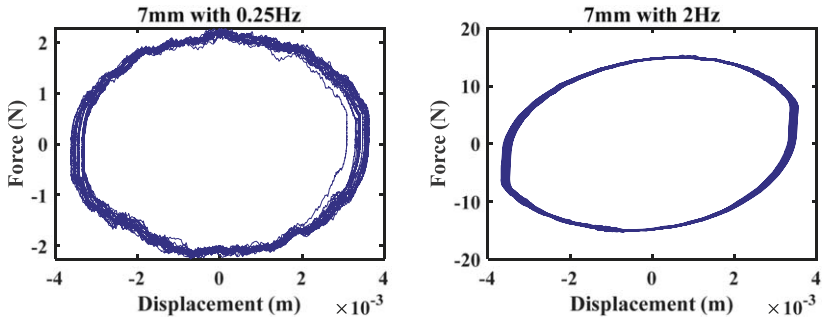

Figure 13. 7 mm Hysteresis loop between force and displacement of ECD performance test.

The purpose of the test was to determine the damping coefficient of the ECD. Assuming the ECD has linear dynamic behaviour, the damping coefficient of each case can be calculated by the division of the force and velocity. To calculate the damping coefficient, figure 12 shows the result of linear regression using the measured data. The distribution of the data exhibits a linear tendency, and the approximate equation is defined as $y = mx$, which is a sloping line equation passing through the zero original point. The slope of the equation describes the damping coefficient of the ECD, which has a damping magnitude of 324.48 $\mathrm{N/(m\,s^{-1})}$.

Figure 13 shows the relationship between the damping force and the 7 mm displacement cases for 0.25 and 2 Hz. Importantly, these hysteresis loops exhibit a somewhat elliptical form, oriented horizontally, which indicates, a device producing pure damping without any additional contribution to stiffness.

The time history response of the 7 mm case is shown in figure 14, which indicates that the reference input and tracking measurement are almost identical, suggesting that the displacement feedforward reference tracking results are satisfactory.

The relevant time history of the damping force output is also shown in figure 14.

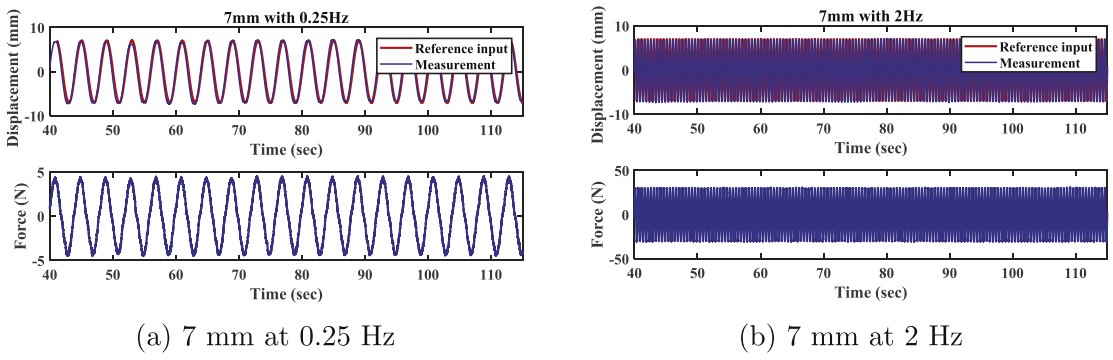

(a) 7 mm at 0.25 Hz (b) 7 mm at 2 Hz

Figure 14. Displacement and damping force time history of the ECD performance test.

A comparison between the results obtained during the performance tests and those from FE simulation can now be made. With reference to the damping force calculation discussed in section 4.1, the vertical alternative pole projection with moving conductive plate in the horizontal direction with fixed velocity of 0.08 m s^{-1} had a damping force of 26.23 N and hence damping coefficient of 327.875 N/(m s^{-1}). In the performance test, the damping coefficient (324.48 N/(m s^{-1})) is close to that obtained in the FE model. Consequently, the analytical calculation and FE simulation appear to provide a satisfactory approximation for the ECD damping force. Although the small error in the analytical calculation might be due to the assumption regarding the uniform distribution of the magnetic flux density, the calculation result is still acceptable for the purpose of predicting the ECD damping.

5. Aluminium moment resisting frame (AMRF) with ECD

5.1. Modal analysis of the AMRF

The ECD prototype construction and performance test were introduced in the previous section. However, the original aim was to evaluate the ECD damper in terms of its vibration suppression ability in conjunction with a civil structure. Therefore, the vertical magnet alternative pole projection ECD was installed on the second level of the AMRF, as shown in figure 15.

The Endevco accelerometers were set up at each level of the AMRF to measure the acceleration in the direction of excitation. The MTS magnetostrictive position sensors were located on the second and third levels to measure the relative one-directional displacement. An Imetrum vision tracking system was also used to detect both horizontal and vertical movement for each level. Finally, an Entran load cell was connected between the copper clamp and L-shape plate to measure the ECD damping force output. The main body of the ECD (magnet and framing) was mounted via the two side angular plates on the second floor. The APS Model 400 shaker was used as the excitation source to provide the input.

Figure 16 shows a photo of the AMRF setup with the ECD installed without its copper plates. The APS shaker was set in the horizontal direction. The armature of the APS shaker was connected to the rigid bar, which is located underneath the second floor, via a load cell.

Initially, the ECD main body (magnet and framing) was mounted on the second floor, without the copper plate inserted into the gap between the magnet panels, so as to avoid any contribution of eddy current damping in the test. A random input was selected to excite the structure. The resulting FRF and phase angle are shown in figure 17.

Table 3 shows the results of the modal testing. The first mode frequency was at 1.81 Hz with damping ratio of 0.35% and modal mass of 37.75 kg. The details for the other modes are also included in the table. The measured mode shapes of each mode during testing are shown in figure 18 (i.e. the first three modes in the first, second and third bendings).

Using the modal testing results, the structural properties can be used to curve- fit the FRF curve of the second level. Figure 19 shows the regenerated and the measured FRF curves. The curve-fitting results appear to be a satisfactory approximation to the real dynamics of the structure. Furthermore, the curve-fitting results can be utilised to implement the ECD design and predict the dynamic performance of the AMRF including the ECD.

5.2. Evaluation of the AMRF with ECD

Once the properties of the bare AMRF model had been established, the insertion of the copper plate into the gap between the magnet panels was carried out, as shown in figure 20.

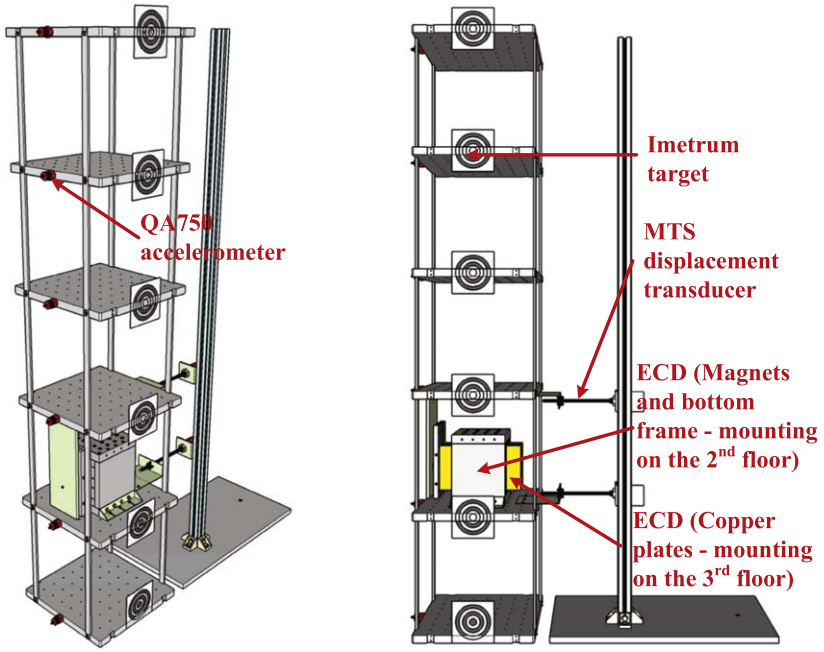

(a) 3D view (b) Front view

Figure 15. Diagram of AMRF with ECD at 2F.

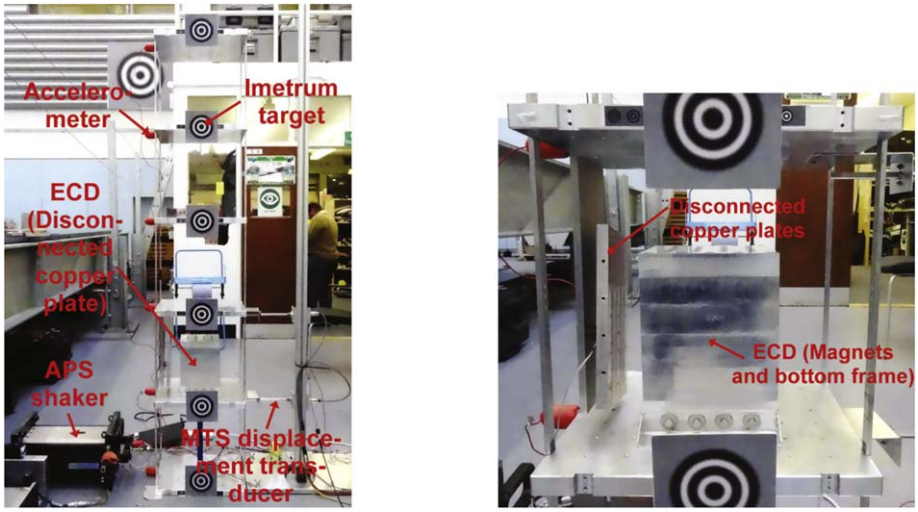

(a) Photo of AMRF with disconnected ECD (b) Photo zoom in of AMRF with disconnected ECD

Figure 16. Photo of the AMRF with disconnected ECD.

To monitor a wide range of frequency responses, a 20 Hz bandwidth random signal was selected to excite the structure. Consequently, figures 21(a) and 22(a) show the sixth and second floor FRF responses obtained following the application of the random input. Clearly, following the installation of the ECD, the FRF amplitude in the entire frequency range undergoes a considerable reduction; for example, with regard to the first mode, the reduction in relation to the sixth floor is 83.62%, while for the second floor it is 82.93%. This suggests that the ECD in this AMRF application is able to provide a reduction of approximately 80%. It is noted that the deflected mode shape of the second bending has one zero magnitude point. In this ECD application, the second mode has a small reduction comparing other modes since the installed location of the damper was between third-second levels, which is the location of zero deflected shape of the second bending.

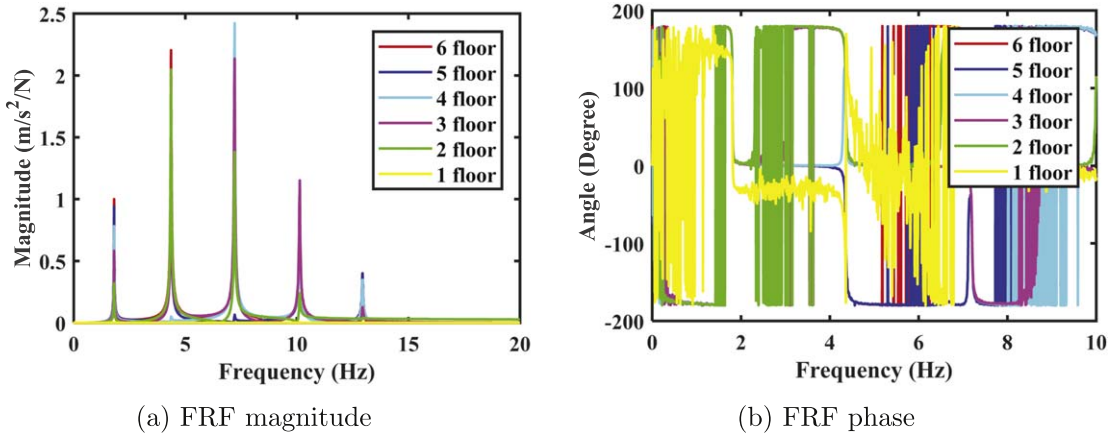

Figure 17. FRF of AMRF with disconnected ECD at 2F.

Table 3. Measured dynamic properties of the six-storey AMRF with disconnected ECD at 2F.

Mode number	Measured natural frequency (Hz)	Damping ratio (%)	Modal mass (kg)
1	1.81	0.35	37.75
2	4.33	0.36	57.63
3	7.05	0.24	46.09
4	9.75	0.24	37.65
5	12.49	0.16	22.36

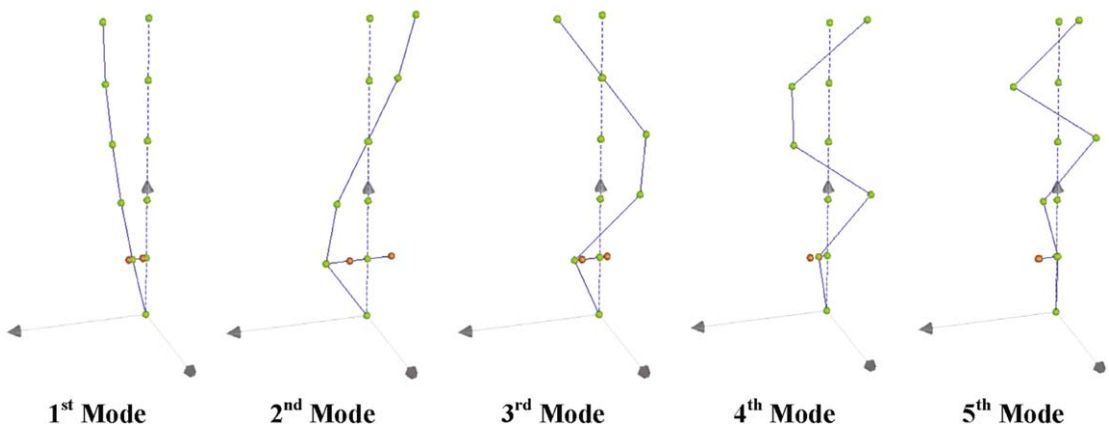

Figure 18. Mode shape of AMRF with disconnected ECD at 2F.

The mode shapes following the installation of the ECD are shown in figure 23. The first mode remained in the first bending mode, the next two modes had undergone a slight change, and the fourth mode seemed to have disappeared.

Following the application of the random input, the structure was then subjected to an input in the form of a chirp signal. The sweeping range of the frequency was from 1.5 to 2.5 Hz, which covers the first mode frequency. Figures 24(a) and (b) show the resulting FRF curves; a significant reduction is evident in the case of the first mode. Figures 25(a) and (b) show the acceleration time history domain of the sixth and second floor. Following the installation of the ECD, a significant reduction can clearly be observed in the case of the acceleration response.

A comparison of the measured acceleration and displacement data, as shown in figures 26(a) and (b), examines the peak magnitude distribution data shown for the top level maximum time step. The relative peak magnitude of acceleration and displacement exhibit a significant reduction following the installation of the

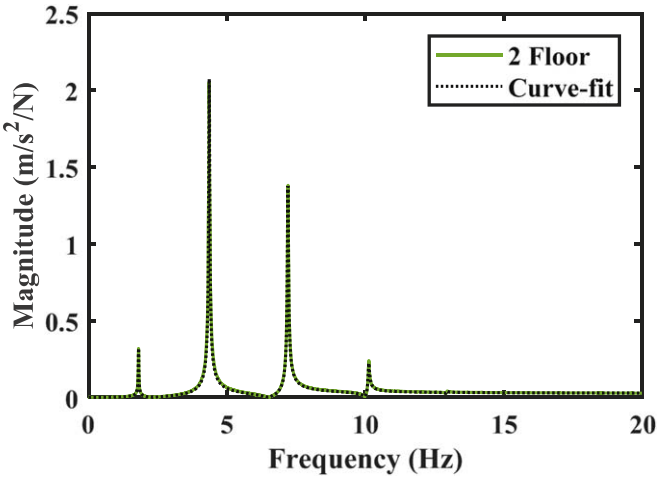

Figure 19. Curve-fitting of AMRF with disconnected ECD at 2F.

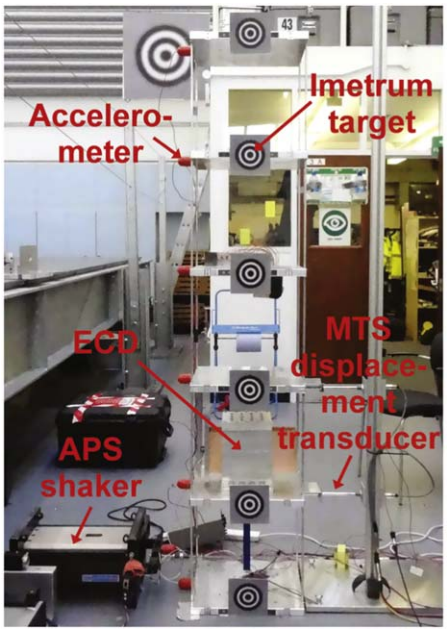

(a) Photo of AMRF with connected ECD at 2F

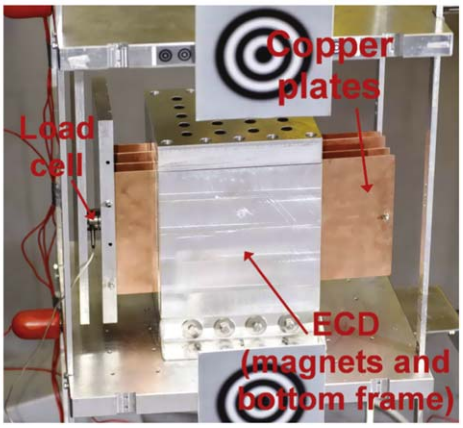

(b) Photo zoom in of AMRF with connected ECD at 2F

Figure 20. Photo of the AMRF with connected ECD.

ECD, which indicates a reduction of approximately 65% in peak response for each level, irrespective of the responses for displacement and acceleration.

Figure 26(c) shows the inter-storey drift ratio of each level. Of all the drift ratios for each level, the largest difference is that obtained in relation to the second floor; 7% (without control) dropping to 2% (following installation of ECD).

The hysteretic relationship between damping force and deformation of the ECD is shown in figure 27. The hysteresis loop reveals a smooth elliptical shape without distortion, indicating the linear dynamic energy dissipation performance of the ECD.

5.3. Evaluation of the simulation and measurement of the AMRF with ECD

Section 4.3 presented the ECD performance test, which allowed the identification of the damping coefficient, and its subsequent incorporation into the ECD design; thus, facilitating the prediction of its dynamic performance. Figure 28 shows a comparison of the simulation and measured results.

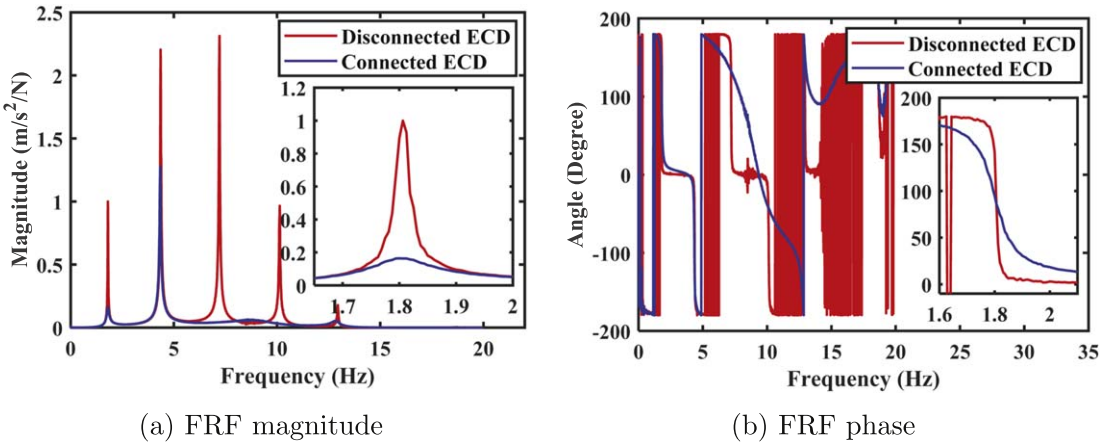

Figure 21. Sixth floor FRF of AMRF with connected ECD.

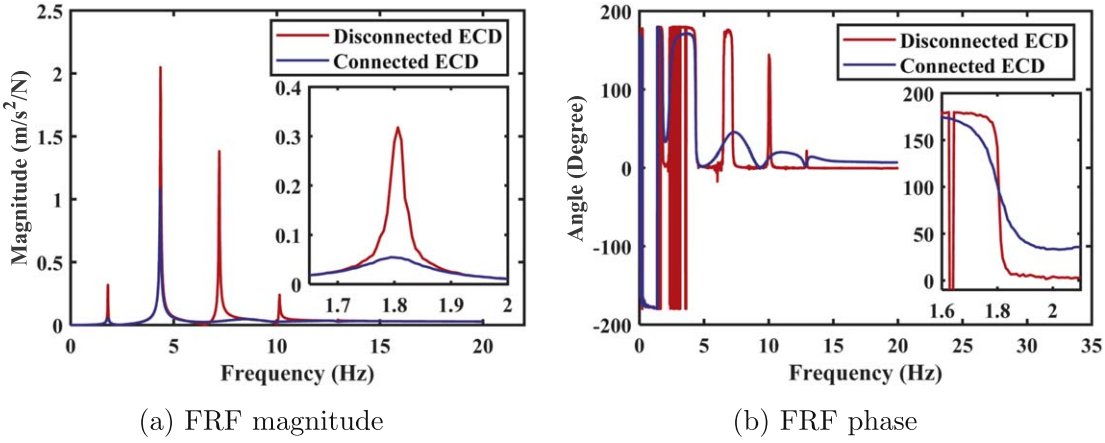

Figure 22. Second floor FRF of AMRF with connected ECD.

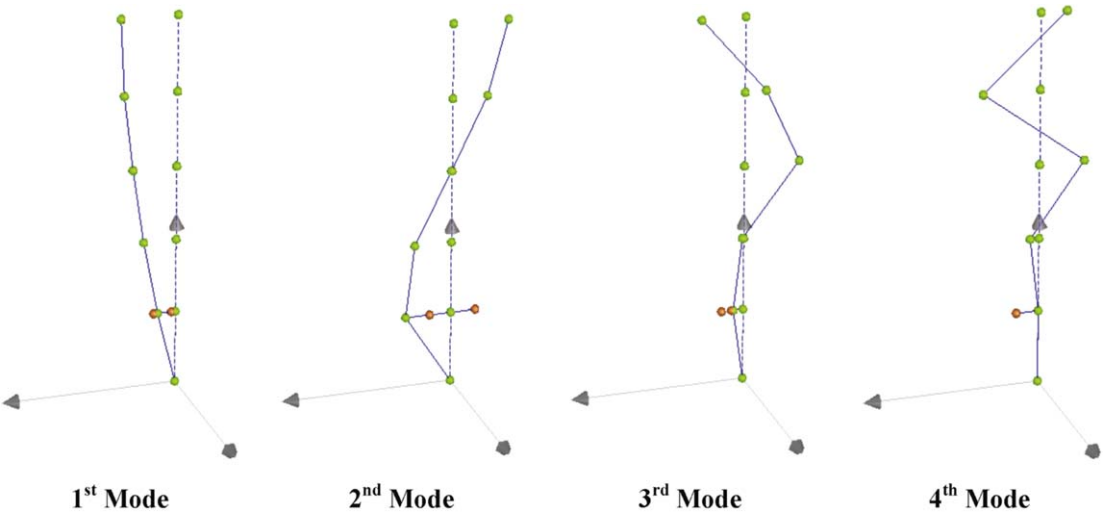

Figure 23. Mode shape of AMRF with connected ECD at 2F.

The FRF measurement without the ECD connected is represented in red, while the regenerated result from estimated parameters of the system, which is a satisfactory approximation, is represented by the first dashed line. Based on the identified system properties, the numerical simulation of the AMRF with ECD connected is

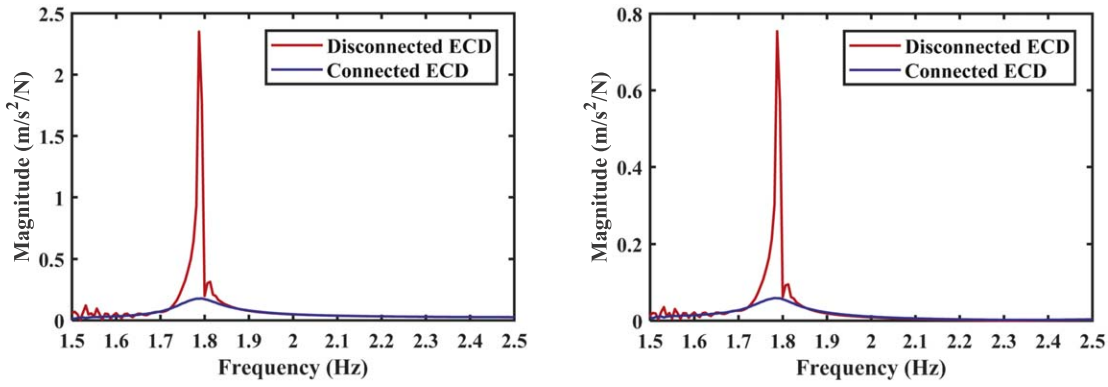

Figure 24. Dynamic response under chirp signal input to AMRF with ECD.

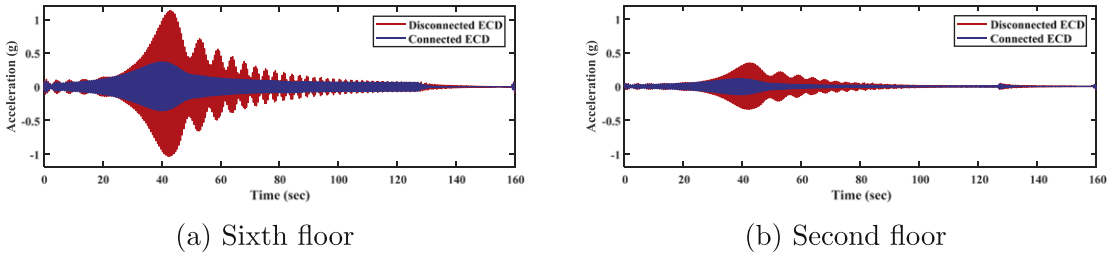

Figure 25. Acceleration time history responses under chirp signal input to AMRF with ECD.

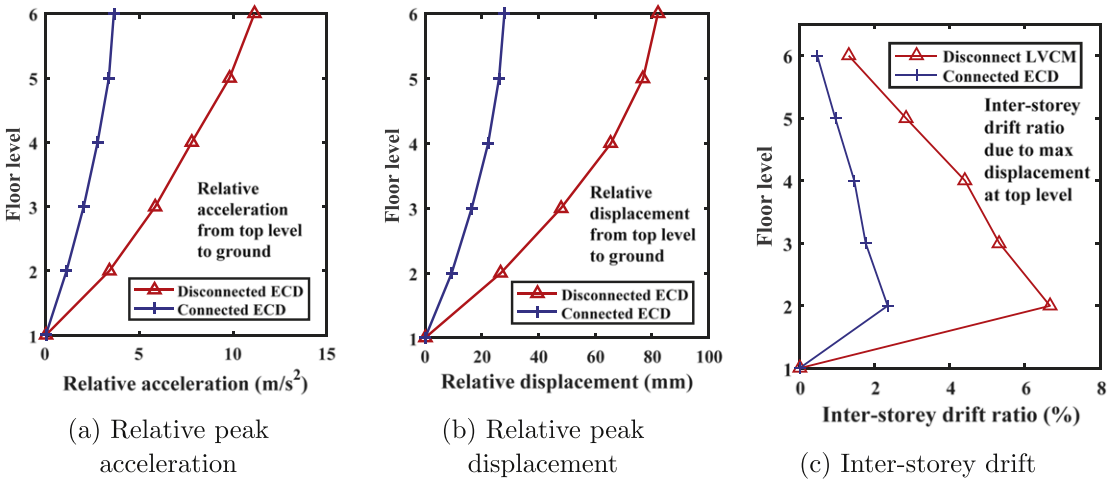

Figure 26. Relative peak acceleration and displacement and inter-storey drift of each level using ECD (picking the time step of maximum response of the 6F).

represented by the second dashed line in figure 28, and the FRF measurement with the ECD connected is represented by the blue line. Overall, it is evident that the numerical simulation can effectively predict the dynamic performance.

A further comparison of the damping force contribution provided by the ECD can be made by using an FEM, as previously described in section 4.1. However, in this case the input velocity to the copper plate was changed to a time-varying velocity, which was calculated by the differentiation of the relative displacement between the second and third floor. Figure 29(a) shows the x, y, z damping force time history components under a chirp signal input. It can be seen that the x component has a larger damping contribution, while the other axes provide almost no damping contribution.

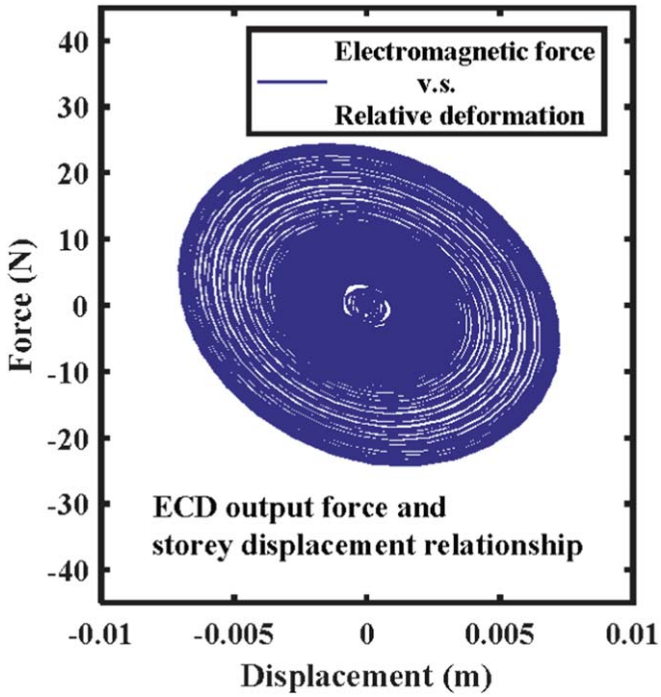

Figure 27. Hysteretic relationship between shear force and relative displacement under chirp signal input to AMRF with ECD.

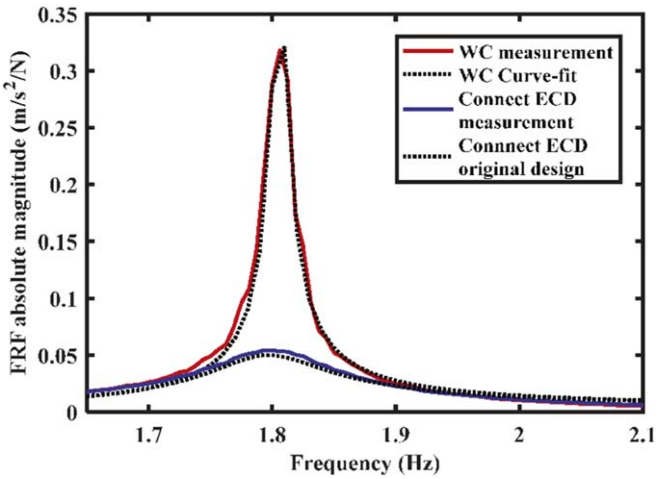

Figure 28. FRF comparison between measured results and simulated design using ECD.

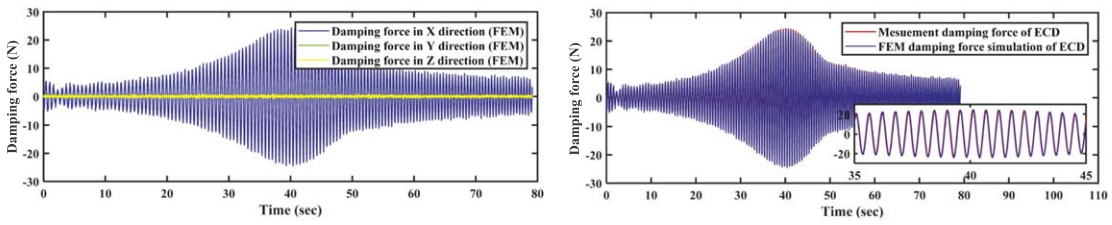

(a) FEM damping force simulation in three axes components

(b) Damping force comparison between the measurement and FEM

Figure 29. The result of the damping force simulation in FEM and comparison with the measurement.

Figure 29(b) shows the comparison between the measurement and FEM of the damping force. It can be seen that the result of the FEM gives a good estimation of the ECD damping force.

Based on the aforementioned discussion, the proposed ECD is able to provide a significant damping contribution for vibration suppression. An advantage of using this ECD is that there is no friction effect in terms of the dynamic performance; therefore, the performance of the ECD is similar to that of an ideal VD, providing a pure damping effect without contributing any additional stiffness. However, this ECD also offers the additional benefit of not being prone to any liquid leakage issues as previously identified in the case of VDs, thus allowing its long-term use in applications, with minimal associated maintenance costs. However, comparing the mass of the ECD (only magnet, copper) and VDs, magnet and copper are lighter materials, which is similar to the weight of the VDs. In this study, the protective mounting frame was made in a large size to surround the magnets, which increased the total weight and geometrical dimension of the ECD. Based on the above evidence regarding the ECD, a case study involving the application of the ECD in conjunction with an TMD to mitigate vibration will be developed, which is discussed in [20, 23].

6. Discussion and conclusions

This study has investigated an alternative damping source, which is electromagnetic damping or eddy current damping. The creation of the damping relies on the electromagnetic coupling effect or electromagnetic induction. Based on the fundamental electromagnetism, the eddy current damping can be calculated. The magnetic pole projection and orientation affects the damping performance. Therefore, both unidirectional and alternative magnetic pole projection have been examined, as were both vertical and horizontal alignments of the magnets. In addition, the moving directions of the conductive material (horizontal and vertical) were also examined via development of analytical expressions for eddy current damping force calculation. Consequently, eight models were built and discussed.

From the original calculation assumption it has been seen that the infinite boundary assumption for current density might give an error on the electromagnetic (damping) force calculation, which might cause over estimation. To overcome this error, the eddy current method of images was introduced and used to calculate the finite boundary electromagnetic (damping) force analytically.

An eddy current damper (ECD) was introduced, including its dimensions and materials. Using this information, the result of the comparison between analytical calculation and FEM showed that the analytical result was reasonably approximate to predict damping force. According to the analysis, if the copper plate moves in the horizontal direction, the configuration of vertical alternative pole projection gives the largest force contribution. Therefore, an ECD prototype was built and implemented for a performance test. It was found that the ECD gave very close to linear damping component. The damping coefficient of the ECD was also validated.

The ECD was installed on the aluminium moment resisting frame (AMRF) for vibration suppression. The ECD was found to achieve over 80% response reduction under random excitation. Under a chirp signal it also had 65% acceleration and displacement reduction. As a result, the ECD in the study can give close to ideal linear damping improvement to the structure. The benefit of the ECD is that it significant has no friction effect and no liquid leaking issue compared to a VD. The strength of the permanent magnet remains for a long time, hence it has low maintenance requirements and provide a feasible damping contribution.

The proposed ECD in this research in comparison with a commercial product of ECD has several of benefits. Firstly, all construction and fabrication error could be easily controlled. Secondly, the copper plate was inserted and moved between each magnet panel, which had no any physical contact and can move smoothly that was approximately avoid the friction issue. Thirdly, the cost of the materials of the damper (magnets and coppers) had a reasonable cost in comparison with the commercial one.

Acknowledgments

The authors would like to acknowledge the financial support provided by UK Engineering and Physical Sciences Research Council (EPSRC) through a Leadership Fellowship Grant (Ref. EP/J004081/2) entitled ‘Advanced Technologies for Mitigation of Human-Induced Vibration’.

ORCID iDs

Wai Kei Ao https://orcid.org/0000-0001-9597-1114

References

[1] Hahn K.D., Johnson E.M., Brokken A and Baldwin S 1998 Eddy current damping of a magnet moving through a pipe *Applied Mathematics and Mechanics* **133** 1066

[2] Nagaya K, Kojima H, Karube Y and Kibayashi H 1984 Braking forces and damping coefficients of eddy current brakes consisting of cylindrical magnets and plate conductors of arbitrary shape *IEEE Transactions on Magnetics* **20** 2136–45

[3] Heald M.A. 1988 Magnetic braking: improved theory *American Journal of Physics* **56** 521

[4] Cadwell L.H. 1996 Magnetic damping: analysis of an eddy current brake using an airtrack *American Journal of Physics* **64** 917

[5] Kapjin L and Kyihwan P 2002 Modeling eddy currents with boundary conditions by using Coulomb's law and the method of images *IEEE Transactions on Magnetics* **38** 1333–40

[6] Cheah S.K. and Sodano H.A. 2008 Novel eddy current damping mechanism for passive magnetic bearings *Journal of Vibration and Control* **14** 1749–66

[7] Chen J-Y, Zhou J-B, Guang Meng and Zhang W-M 2009 Evaluation of eddy-current effects on diamagnetic bearings for microsystems *IEEE Transactions on Industrial Electronics* **56** 964–72

[8] Ellis R, Fink R and Rich R 1989 Eddy current damper *NASA, Marshall Space Flight Center, The 23rd Aerospace Mechanisms Symposium* **1** 127–38

[9] Ebrahimi B, Khamesee M.B. and Golnaraghi M.F. 2008 Design and modeling of a magnetic shock absorber based on eddy current damping effect *Journal of Sound and Vibration* **315** 875–89

[10] Ebrahimi B, Khamesee M.B. and Golnaraghi M.F. 2009 A novel eddy current damper: theory and experiment *Journal of Physics: Applied Physics* **42** 7075001

[11] Tonoli A, Amati N and Silvagni M 2008 Transformer eddy current dampers for the vibration control *Journal of Dynamic Systems, Measurement, and Control* **130** 9031010

[12] Laborenz J, Siewert C, Panning L, Wallaschek J and Gerber C 2010 Eddy current damping: A concept study for steam turbine blading *Journal of Engineering for Gas Turbines and Power* **132** 7052505

[13] Gou X-f, Yang Y and Zheng X-j 2004 Analytic expression of magnetic field distribution of rectangular permanent magnets *Applied Mathematics and Mechanics* **25** 297–306

[14] Zuo L, Chen X and Nayfeh S 2011 Design and analysis of a new type of electromagnetic damper with increased energy density *Journal of Vibration and Acoustics* 041006

[15] Bae J-S, Kwak M.K. and Inman D.J. 2005 Vibration suppression of a cantilever beam using eddy current damper *Journal of Sound and Vibration* **284** 805–24

[16] Sodano H.A. and Inman D.J. 2007 Non-contact vibration control system employing an active eddy current damper *Journal of Sound and Vibration* **305** 596–613

[17] Yang Y, Xu D and Liu Q 2015 Milling vibration attenuation by eddy current damping *The International Journal of Advanced Manufacturing Technology* **81** 445

[18] Wang Z, Chen Z and Wang J 2012 Feasibility study of a large-scale tuned mass damper with eddy current damping mechanism *Earthquake Engineering and Engineering Vibration* **11** 391–401

[19] Bourquin F, Caruso G, Peigney M and Siegert D 2014 Magnetically tuned mass dampers for optimal vibration damping of large structures *Smart Materials and Structures* **23** 8085009

[20] Ao W.K. 2018 Electromagnetic damping for control of vibrations in civil structures *The University of Exeter PhD Thesis* Exeter, Devon, United Kingdom

[21] Pluk K.J.W., van Beek T.A., Jansen J.W. and Lomonova E.A. 2014 Modeling and measurements on a finite rectangular conducting plate in an eddy current damper *IEEE Transactions on Industrial Electronics* **61** 4061–72

[22] Goodwin G.C., Graebe S.F. and Salgado M.E. 2001 *Control Systems Design* (United States of America: Prentice Hall)

[23] Ao W.K. and Reynolds P 2017 Analytical and experimental study of eddy current damper for vibration suppression in a footbridge structure *Proceedings of IMAC-XXXV Congress, Hyatt Regency Orange County, Garden Grove, California, USA*